JGR Atmospheres

RESEARCH ARTICLE
10.1029/2021JD036198

Identifying Eastern US Atmospheric River Types and Evaluating Historical Trends

Craig A. Ramseyer[1], Tyler J. Stanfield[1], Zachary Van Tol[2], Tyler Gingrich[1], Parker Henry[1], Peter Forister[1], Bradley Lamkin[3], Shakira Stackhouse[1], and Samrin Samaiya Sauda[1]

[1]Department of Geography, Virginia Polytechnic Institute and State University, Blacksburg, VA, USA, [2]School of Sustainability, Arizona State University, Tempe, AZ, USA, [3]School of Meteorology,, University of Oklahoma, Norman, OK, USA

Abstract An atmospheric river (AR) is the primary moisture transport forcing in the Western United States, making ARs the predominant producer of extreme precipitation events in this region. A growing body of evidence suggests similar impacts for the Central and Eastern US This study determines the most prominent types of ARs in the Central and Eastern US study domain through the implementation of a machine learning methodology. Self-organizing maps (SOMs) are leveraged to determine what "flavors" of ARs exist in the study domain. Four atmospheric river detection criteria are utilized to investigate the variability AR types. Mann-Kendall trend analyses on AR strength and size are produced to evaluate changes over the study period. The results confirm extratropical cyclones as the most common driver of ARs, however, limited kinematic forcing can also instigate the development of AR events. Results show coastal cyclones and lee-side cyclones are responsible for producing the strongest ARs. The trend analysis results suggest that ARs associated with Nor'easters and ARs originating in the Gulf of Mexico are exhibiting increasing trends in intensity and/or size. Increasing moisture transport by mature cyclones across the Central and Eastern US have important implications for flooding in highly populated corridors. Areas of concern include the Northeast and Southeast US, while localized enhancement of rainfall is seen along the eastern and southern slopes of the Appalachian Mountains. In addition to the physical findings, this research highlights the importance and sensitivity of statistically significant results to the specific atmospheric river detection criteria that was leveraged.

Plain Language Summary Atmospheric rivers (ARs) are a primary driver of moving moisture through Earth's atmosphere usually by winds produced by large, non-tropical cyclones. In the United States (US), ARs have been linked with extreme rainfall events and flooding. This study investigates the different "types" or "flavors" of ARs in the Central and Eastern US, where AR-focused studies are less numerous than the Western US Self-organizing maps (SOMs), a form of machine learning, are built to determine the AR types. Additionally, an analysis is conducted on the strength and size of ARs to determine if they are changing the amount of moisture being moved over the 41-year study period. The SOMs confirm non-tropical cyclones as the primary producer of strong ARs with "Nor'easter" cyclones and cyclones forming over the Upper Midwest producing the strongest ARs. The results suggest that strong cyclones are transporting increasing amounts of moisture, via ARs, through the study period. Increasing trends in AR transport across the Central and Eastern US have important implications for flooding in highly populated corridors, including the Northeast and Southeast US.

Key Points:

- Self-organizing maps are effective at detecting atmospheric rivers in the Eastern US, the strongest of which are produced by extratropical cyclones
- Atmospheric rivers associated with strong coastal cyclones show statistically significant increasing moisture transport
- Strong atmospheric rivers rooted in the Gulf of Mexico or Gulf Stream lead to the most intense rainfall and are situated over large population centers

Supporting Information:

Supporting Information may be found in the online version of this article.

Correspondence to:

C. A. Ramseyer,
ramseyer@vt.edu

Citation:

Ramseyer, C. A., Stanfield, T. J., Van Tol, Z., Gingrich, T., Henry, P., Forister, P., et al. (2022). Identifying Eastern US atmospheric river types and evaluating historical trends. *Journal of Geophysical Research: Atmospheres*, *127*, e2021JD036198. https://doi.org/10.1029/2021JD036198

Received 11 NOV 2021
Accepted 28 AUG 2022

Author Contributions:

Conceptualization: Craig A. Ramseyer, Tyler J. Stanfield, Zachary Van Tol, Tyler Gingrich, Parker Henry, Peter Forister, Shakira Stackhouse, Samrin Samaiya Sauda
Data curation: Craig A. Ramseyer
Formal analysis: Craig A. Ramseyer, Tyler J. Stanfield, Bradley Lamkin
Investigation: Craig A. Ramseyer
Methodology: Craig A. Ramseyer, Tyler J. Stanfield, Zachary Van Tol, Tyler Gingrich, Parker Henry, Bradley Lamkin
Resources: Craig A. Ramseyer

1. Introduction

Atmospheric rivers (ARs) are a meteorological phenomenon receiving increasing attention due to their role in the redistribution of moisture across the globe and their connection to high-impact weather events, in particular, flooding (Corringham et al., 2019; Dettinger et al., 2011; Eiras-Barca et al., 2016; Hirota et al., 2016; Kirien et al., 2020; Lavers & Villarini, 2015; Mo & Lin, 2019; Moore et al., 2012; Nayak & Villarini, 2017; Neiman et al., 2008; Pasquier et al., 2019). On average, ARs are responsible for transporting more than double the flow of the Amazon River, making them the largest freshwater "rivers" on Earth (Zhu & Newell, 1998). These atmospheric phenomena typically have a length at least two times that of their width and are most commonly associated with tropical moisture sources via southerly flow in the low-level jet (Dettinger et al., 2011; Edwards et al., 2020; Ford et al., 2015; Higgins et al., 2011; Mestas-Nuñez et al., 2007; Moore et al., 2012; Nayak & Villarini, 2017; Newell et al., 1992; Slinskey et al., 2020). The most commonly utilized metrics to detect ARs are integrated

Software: Craig A. Ramseyer, Bradley Lamkin
Supervision: Craig A. Ramseyer
Validation: Craig A. Ramseyer
Visualization: Craig A. Ramseyer
Writing – original draft: Craig A. Ramseyer, Tyler J. Stanfield, Zachary Van Tol, Tyler Gingrich, Parker Henry, Peter Forister, Bradley Lamkin, Shakira Stackhouse, Samrin Samaiya Sauda
Writing – review & editing: Craig A. Ramseyer, Tyler J. Stanfield, Zachary Van Tol, Tyler Gingrich, Parker Henry, Peter Forister, Shakira Stackhouse

water vapor (IWV) and integrated vapor transport (IVT). While IWV quantifies the amount of liquid present in a given atmospheric column if all of the water vapor was condensed, IVT includes both integrated moisture and the horizontal wind vectors to quantify moisture advection.

Thresholds for AR detection using IVT in the mid-latitudes vary throughout the literature, with most early studies utilizing a threshold of 250 kg $m^{-1}s^{-1}$ when integrated from 1,000 mb to 300 mb (Brands et al., 2017; Dacre et al., 2015; Gershunov et al., 2017; Ralph & Dettinger, 2011; Rutz et al., 2014). Over time, stricter definitions for the IVT threshold have evolved with recent studies using IVT thresholds as high as 500 kg $m^{-1}s^{-1}$ (Leung & Qian, 2009) and exceeding 700 kg $m^{-1}s^{-1}$ (Sellars et al., 2015). In addition to the metrics discussed above, new research is also investigating the use of machine learning models to automate atmospheric river detection (Prabhat et al., 2021). New methodologies are developing algorithms to track AR cores in an attempt to track the lifecycle of global midlatitude ARs and associated precipitation (Shearer et al., 2020). Further, relative methods for defining IVT thresholds based on background moisture have been employed (e.g., Guan & Waliser, 2015; Lavers et al., 2012; Lora et al., 2017; Mo et al., 2021).

In response to the rapidly expanding scope of AR research, and the detection algorithms built to study them, the Atmospheric River Tracking Method Intercomparison Project (ARTMIP) was initiated to evaluate uncertainties that arise from atmospheric river detection tool (ARDT) selection (Shields et al., 2018). ARTMIP investigates the sensitivity of AR detection and statistics to the ARDT utilized in research studies (Chen et al., 2018; Ralph et al., 2019; Rutz et al., 2019). Uncertainties exist in AR counts, seasonality, trends, and statistical properties based on the ARDT used in a particular study (Collow et al., 2022; Inda-Díaz et al., 2021; Lora et al., 2020; O'Brien et al., 2020; Zhou et al., 2021). The ongoing ARTMIP develops best practices when conducting AR research that leverages ARDTs, including creating methodologies employing more than one ARDT to better assess the statistical uncertainties that arise from selecting ARDTs (e.g., Rutz et al., 2019). The ARTMIP also highlights the sensitivity of precipitation trends elucidated by methodologies employing ARDTs (Collow et al., 2022). Many of the methodological decisions presented in this study are informed by the findings of ARTMIP.

Most of the early AR literature focuses on ARs that affect the western United States, where these features contribute to significant amounts of the annual precipitation budget, especially during the cool season. Despite this geographical focus, ARs can also have a significant impact on precipitation in the central and eastern United States during the cool and warm seasons (Dirmeyer & Kinter, 2009, 2010; Lavers & Villarini, 2013, 2015; Mestas-Nuñez et al., 2007; D. K. Miller et al., 2019; Moore et al., 2012). Studies have shown that a higher IVT threshold should accompany this shift in geographic domain as the Central and Eastern U.S retain elevated background (e.g., climatological) moisture compared to the US West Coast. The median IVT for a study examining the United States east of the Rockies was shown to be 350 kg $m^{-1}s^{-1}$ (Lavers & Villarini, 2015). Other research has demonstrated the need for higher IVT thresholds in the Eastern US, as the 95th percentile across studies is approximately 550 kg $m^{-1}s^{-1}$ (Mahoney et al., 2016; D. K. Miller et al., 2019; Teale & Robinson, 2020, 2022). In contrast to the west coast, where IVT gradients typically run west-to-east, ARs east of the Rockies usually exhibit a stronger north-south IVT gradient (Slinskey et al., 2020). This directional component dictates that, rather than orographic lifting, AR events run parallel to the Appalachian Mountains prescribing frontal lifting as the predominant mechanism for enhanced precipitation (Slinskey et al., 2020).

Impacts from ARs in the Central and Eastern US include flooding, mudslides, and increased precipitation (D. K. Miller et al., 2019; Nayak & Villarini, 2017). Approximately 30%–35% of annual rainfall over the southeast and central United States can be attributed to AR activity (Debbage et al., 2017; Lavers & Villarini, 2015; Nayak & Villarini, 2017). In some regions of the central United States, up to 70% of flooding events can be ascribed to AR activity (Nayak & Villarini, 2017; Slinskey et al., 2020). Most of the rainfall from ARs occur within 150 km of the major axis of the "river" where rainfall has shown a positive relationship with the magnitude of water vapor transport (Nayak & Villarini, 2017). Over the central United States, the magnitude of AR related rainfall has shown a significant relationship with IVT magnitude (Nayak & Villarini, 2018). Recently, patterns of moisture transport across the Eastern US have been shown to be increasing the frequency and intensity of extreme rainfall events (Teale & Robinson, 2022).

This study will expand the AR literature by:

1. diagnosing the types of ARs in the Eastern and Central US through the implementation of self-organizing maps (SOMs), a machine learning methodology;

2. determining which ARDT criteria are appropriate to resolve the continuum of ARs that occur in the study domain;
3. identifying which AR types are strongest by examining a suite of statistical properties for each AR type;
4. leveraging Mann-Kendall trend analyses to investigate changes in the size and intensity of each AR type;
5. elucidating whether the AR types are efficient in producing spatially coherent rainfall from moisture transport.

2. Data and Methods

The variables used in this study were those needed to derive IVT (u-wind, v-wind, specific humidity) and mean sea level pressure from the ECMWF ERA5 weather reanalysis data set. The ERA5 global reanalysis data set is the fifth generation in atmospheric reanalysis products produced by ECMWF and replaces the ERA-Interim reanalysis data set (Dee et al., 2011). ERA5 uses the Integrated Forecast System (IFS) release 41r2 which includes numerous model improvements and has led to major advances in the ability to assimilate satellite data (Hersbach et al., 2020). These advances in ECMWF reanalysis data make ERA5 an appropriate data set for analyzing spatially continuous moisture fields such as those used to diagnose ARs. This data set provides hourly data on surface and upper-air parameters at a notably finer spatiotemporal resolution compared to prior generations of weather reanalysis datasets. With an approximately 31 km global resolution (TL639), ECMWF consists of 137 atmospheric levels, going up to 0.01 hPa. For this study, ERA5 data–interpolated onto pressure levels–were utilized for the temporal period of 1979–2020. ERA5 has been shown to resolve ARs well, relative to other global reanalysis products, particularly due to its ability to resolve narrow, filament structures related to maximum moisture transport within the core of ARs (Collow et al., 2022). The spatial domain was determined by capturing the areas in Central and Eastern US prone to strong moisture advection out of the Gulf of Mexico and Gulf Stream and tropical North Atlantic (Figure 1a).

Equation 1 shows the AR detection calculation used in this study where IVT is derived using the ERA5 pressure level data from 1,000 to 300 hPa where g is gravity, q is specific humidity, and V is the wind vector derived from the u- and v-wind at each pressure level (Ralph et al., 2017):

$$\mathrm{IVT} = \frac{1}{g}\int_{1000\,\mathrm{hPa}}^{300\,\mathrm{hPa}} qV\,dp. \tag{1}$$

Pressure levels occur every 25 hPa from 1,000 to 750 hPa and increase to every 50 hPa from 750 to 300 hPa. The ERA5-derived IVT data set used in this study has been made publicly available by the authors (Ramseyer, 2021). This break down results in the utilization of 20 pressure levels for the IVT calculation. While IVT is often calculated up to 300 hPa, it is worth pointing out that most of the moisture transport (e.g., 95%) occurs in the lowest 3 km of the troposphere (Ralph et al., 2017, 2018).

Before implementing the ARDT with the IVT data, the IVT climatology was updated to remove temporal periods where a tropical cyclone circulation was detected in the study domain. This was accomplished by identifying all of the tropical cyclone tracks from the Hurricane Database 2nd Generation (HURDAT2) that intersected with the study domain (Landsea & Franklin, 2013). Once those tropical cyclones were identified, any ARs that occurred concurrently were removed from the study period's data set. This methodological step ensures that none of the ARs identified by the ARDT thresholds are caused or influenced by tropical cyclones, helping to isolate ARs generated primarily from mid-latitude forcing mechanisms.

Due to the elevated background moisture over the Eastern US, this study does not implement a 250 kg $m^{-1}s^{-1}$ IVT threshold. To validate the elimination of the ARDTs that utilize a minimum IVT threshold of 250 kg $m^{-1}s^{-1}$, ARDT thresholds with both the traditional metric (>250 kg $m^{-1}s^{-1}$) and stricter definitions (>500 kg $m^{-1}s^{-1}$) are employed in this study. Over 50% of the 6-hr reanalysis data over the study period was identified to have an AR for the 250 kg $m^{-1}s^{-1}$ definition (with a 1,500 km length threshold) while less than 10% of the observations were found to have an AR using a 500 kg $m^{-1}s^{-1}$ threshold (with a 1,500 km length threshold). The stricter definition thus limits ARs to the strongest events and more appropriately aligns with traditional definitions of ARs as strong, anomalous moisture transport events. Thus, this analysis establishes that it is appropriate to employ a lower bound of 500 kg $m^{-1}s^{-1}$ for all detection criteria used in this study.

In addition to letting the AR literature guide the ARDT selection criteria for this study domain, the 95th percentile ERA5 IVT for all grid points was calculated to determine what constitutes an extreme IVT value (Figure 2). This

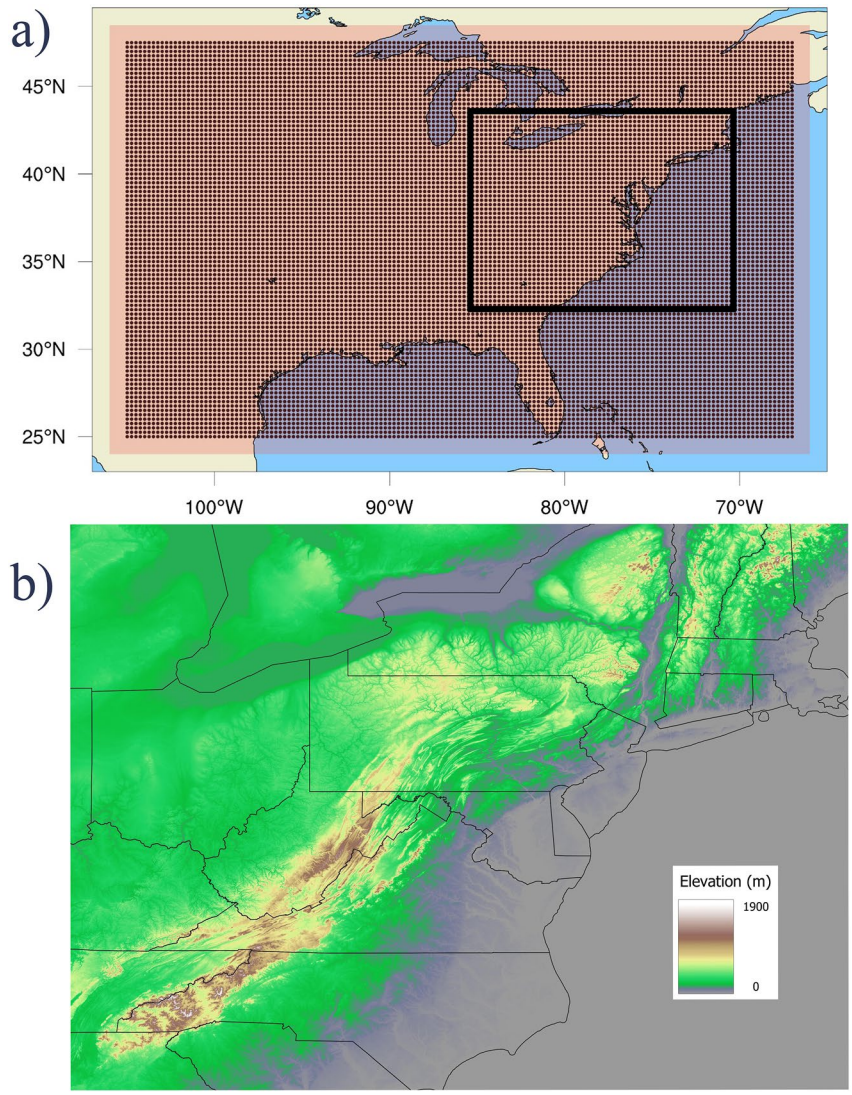

Figure 1. (a) ERA5 grid points (0.25° × 0.25° spatial resolution) in the study domain used in the calculation of integrated vapor transport. (b) 7.5-arc-second Global Multi-Resolution Terrain Elevation Data highlighting the study subdomain (black rectangle in Figure 1a) with greatest varying topography.

analysis illustrates the spatial patterns of IVT with a particular emphasis on the influence of the Gulf of Mexico and the Gulf Stream on IVT in the study domain. Most of the study domain experiences a 95th percentile IVT of at least 500 kg $m^{-1}s^{-1}$ with sharp gradients in the Great Plains and at latitudes north of 45°. Over the Gulf Stream (and immediately downwind), the 95th percentile increases to over 700 kg $m^{-1}s^{-1}$.

An ARDT framework, with four different threshold criteria, is used in this study Ramseyer, 2022. We implement a 750 kg $m^{-1}s^{-1}$ threshold on two of the ARDT members to look at the strongest ARs that may occur over the Gulf Stream (Table 1). Setting IVT criteria based on the 95th percentile of the IVT climatology presented in Figure 2 follows literature that utilizes relative IVT thresholds based on domain-specific background moisture (e.g., Guan & Waliser, 2015; Lavers et al., 2012; Lora et al., 2017; Mo et al., 2021). All four of the ARDT members use a contiguous IVT length scale of at least 1,500 km. The 1,500 km length scale threshold has been used in other AR studies in the southeast US and is investigated here as the minimum threshold (D. K. Miller et al., 2019).

In order to determine the common types of ARs in the study domain, SOMs are utilized. SOMs are commonly used in the field of synoptic climatology (Cassano et al., 2015; Hewitson & Crane, 2002; Mattingly et al., 2016; Morioka et al., 2010; Sheridan & Lee, 2011). SOMs implement a neural network to identify a distribution function

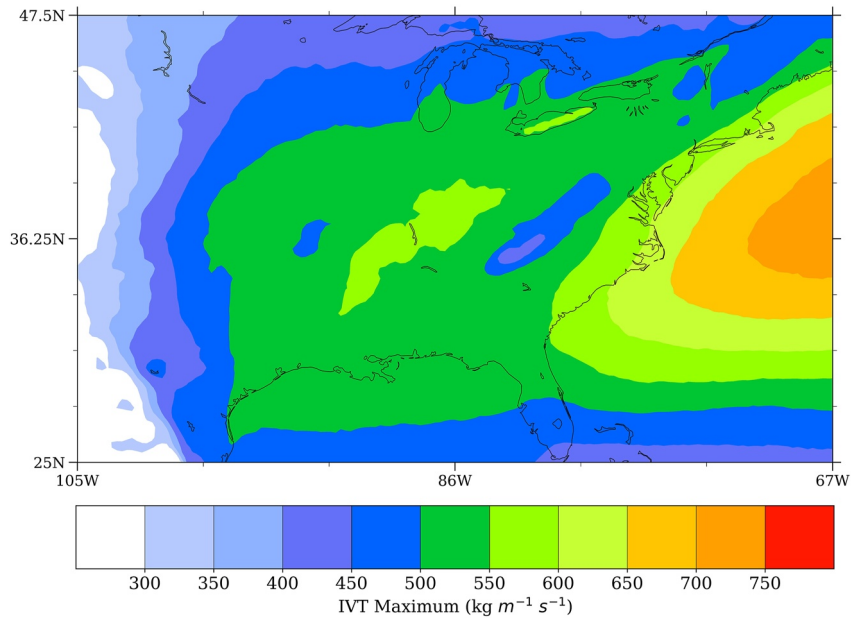

Figure 2. The 95th percentile integrated vapor transport for the study period in the study domain establishing the basis for the absolute thresholds chosen in Table 1.

that best fits the data based on a prescribed threshold and a user-defined set of nodes that identify values most representative (of the particular event of interest) from the broader data set (Sheridan & Lee, 2011). Whereas dimensionality reduction methods (e.g., principal component analysis) can result in some input vectors not being represented, the self-organized map (SOM) allows for the inclusion of all input vectors (e.g., 6-hourly IVT data) in the final model. The user-defined nodes are initialized into the data space before training begins. As the model iteratively updates, the nodes relocate in the input data space in an attempt to minimize error between the nodes and the input vectors.

In this study, the input vectors are the 6-hr ERA5 derived IVT values for all grid points in the study domain during periods when AR criteria was met. This study utilizes 6-hourly data to allow for the AR to sufficiently change from each observation to the next. This also limits overweighting ARs that may be of longer duration or slow to evolve. The SOM treats each time step as an input vector. Thus, if using hourly data, longer-duration and slow-moving ARs would be weighted more heavily and could reduce the ability of the SOM to resolve shorter duration ARs.

At the end of training, each input vector is mapped to its best-matching units (BMUs) where the first of the BMUs is effectively the nearest node to that vector in the data space. The mean for all of the input vectors can be calculated to find a representative mean-state for each of the nodes. In the case of this study, representative mean-states for each node depict an AR type or "flavor." Alternatively, the input vector closest to the mean-state can also be used to represent each node. Of particular interest in this study are the mean IVT and mean sea-level pressure states for each of the AR types. This allows for visualization of the size and intensity of each AR type, while also investigating the kinematic drivers of each AR type as deduced by the MSLP mean-states. Since the temporal data for the input vectors are retained, the trends of AR strength and size metrics can also be explored.

Table 1
Overview of the ARDT Criteria Employed in the Study and the Number of ARs Detected in the 42-Year Climatology

ARDT name	IVT threshold	Length (km)	ARs detected
ARDT5	500 kg m^{-1} s^{-1}	1,500	5,677
ARDT5-2	500 kg m^{-1} s^{-1}	2,000	1,286
ARDT75	750 kg m^{-1} s^{-1}	1,500	488
ARDT75-2	750 kg m^{-1} s^{-1}	2,000	44

After testing a suite of SOM node maps, six nodes on a hexagonal lattice, were selected for this study. The 6-node SOM represents a spectrum of AR types while producing little redundancy, which allows for sufficient mapping of observations to each node and permits a more robust trend analysis. The mean IVT states of another SOM is provided as Figure S1in Supporting Information S1. A test run using 12- and 18-node SOMs using ARDT5 produced too many similar AR types, and led to some of the node types having limited numbers of observations. The trend analyses for the 12-node SOM (Figure S2

in Supporting Information S1) and the 18-node SOM showed similar trends as the 6-node ARDT5 SOM, which suggests the number of nodes selected in the SOM does not influence the overarching results and conclusions presented in this study. Another advantage of the 6-node SOM is the ability in depth investigation of each of the AR types. Larger SOMs–merely due to the amount of nodes– preclude discussion on all of the AR types resolved by the model.

Lastly, we propose the use of a "nested SOM" approach to analyze the inter-node variability of particularly interesting AR types. These SOMs, referred to as "nested SOMs" hereafter, allow for better resolution of less frequent or more extreme types of ARs that may be driving any trends elucidated in the trend analyses.

The training of the SOMs was conducted using the SOM Toolbox, version 2.1 (Vesanto et al., 2000). The final SOMs presented here were created using sequential training and a lattice node structure. The lattice node structure is selected here following best practices of SOM training as lattice structures ensure that adjacent nodes are equidistant from one another, something not achieved by rectangular node structures (Vesanto et al., 2000).

The results from three SOMs (ARDT5, ARDT5-2, ARDT75) were then tested for any statistically significant trends in intensity and size of node types using Mann-Kendall tests (Kendall, 1948; Mann, 1945). The results from ARDT75-2 were not used to train a SOM due to the limited number of ARs detected using that algorithm (e.g., $N = 44$).

The maximum IVT and mean IVT were calculated to analyze intensity, while the size of the AR was computed using the AR length. Maximum IVT is calculated using a nine-grid point mean, centered on the grid point with the highest IVT within the core of the AR. Mean IVT is calculated by taking the mean of all grid points within the AR (e.g., area of contiguous grid points exceeding the 500 kg $m^{-1}s^{-1}$ threshold). This metric provides analysis on changes to the mean state of the entire AR. Lastly, the length of each AR is established by determining the length of the contiguous ERA5 grid points surpassing the IVT threshold. This metric allows for a quantitative assessment of the size of AR.

Lastly, Parameter-elevation Relationships on Independent Slopes Model (PRISM) version 4 daily precipitation data are used to investigate which AR types actualize the increased moisture transport into precipitation (Daly et al., 2021). PRISM data are available on a 4-km grid, making them acceptable for use in areas of varying topography such as the Appalachian Mountains. This data product provides more detailed information at high elevations that would be underrepresented on the ERA5 $0.25° \times 0.25°$ precipitation estimates. For each node, the mean-state for PRISM precipitation is produced using the temporal data for all input-vectors mapping to each node. This yields a mean precipitation state for each AR type.

3. Results

3.1. Results From the ARDT

All four thresholds used in the ARDT framework were run on the 6-hourly IVT fields for the entire temporal period from 1979 to 2020 resulting in >63,000 possible time steps with ARs. This number was reduced slightly after removing time steps where a tropical cyclone was present in the study area, as outlined in the methodology. Table 1 presents each of the criteria implemented in the ARDT framework tested in this study and the number of ARs detected by each of the studies. ARDT5 identified 5,677 ARs in the study period, representing 9% of all available time steps. Increasing the length threshold in ARDT5-2 resulted in 1,286 ARs, which represents an 78% reduction in the number of ARs detected compared to ARDT5.

When increasing the IVT threshold to 750 kg m^{-1} s^{-1}, the number of ARs detected further decreases to 488 for ARDT75 and 44 for ARDT75-2. These represent order of magnitude decreases from ARDT5 and ARDT5-2. As our study period covers 41 years, ARDT75 only detects approximately 12 ARs per year in the study area, while ARDT75-2 detects an average of 1 AR per year.

A Mann-Kendall test was conducted to analyze the change in frequency across the 41-year climatology. This test was not conducted on the ARDT75-2 ARs, as the sample size was insufficient. All three Mann-Kendall tests revealed positive trends in annual AR frequencies but none of the three were statistically significant at the $p < 0.05$ threshold. The ARDT5 and ARDT5-2 showed the strongest increases with p-values of 0.11 and 0.15 respectively.

3.2. SOM and Mann-Kendall Results From ARDT5, ARDT5-2, and ARDT75

In order to evaluate each of the SOMs from the three ARDT criteria uniformly, the same number of nodes were utilized. As ARDT75 detected 488 ARs, SOMs utilizing more than six nodes could result in some nodes with fewer than 50 observations over the 41-year climatology– at this point, any trends detected would yield statistically dubious results. Additionally, keeping the node count low allows for more detailed analyses of each node within the limits of the manuscript. All three SOMs were trained using a hexagonal lattice with a map size of 2×3 and were trained for 1,000 iterations to allow for the minimization of error to reach a global, not local, minimum.

Figure 3 illustrates the composite IVT for each of the six AR types elucidated by the three SOMs. These figures are accompanied by statistical output from the Mann-Kendall test examining the change in maximum IVT over the study period. The ARDT5 SOM, trained with 5,677 ARs, identifies six AR types that vary in the orientation of the primary moisture axis. Some (nodes 3 and 5) are oriented more zonally, indicating the AR is primarily forced by the u-component of the wind field (Figure 3a). Nodes 1, 2, 4, and 6 have increased meridional forcing, driven increasingly by the v-component of the wind. These patterns are likely associated with the warm-conveyor belt and/or the low-level jet driven by mid-latitude cyclogenesis (Dacre et al., 2019). However, even these four nodes display a more SW-NE orientation, indicating some forcing from the u-component of the wind. Nodes 1, 2, and 4 have the strongest composite IVT, with peak values exceeding 700 kg $m^{-1}s^{-1}$. The results of the Mann-Kendall test indicate increasing trends in all nodes 1–5 with all five nodes exhibiting a statistically significant trend at the $p < 0.05$ significance level.

The SOM for ARDT5-2 also reveals large variability in the types of ARs where the primary moisture axes can be both zonally and meridionally oriented (Figure 3b). Three AR types are primarily meridional in orientation (nodes 1, 4, and 6) and three AR types that are dominated by the zonal component of the kinematic field (nodes 2, 3, and 5). Nodes 1 and 4 show the strongest composite IVT, with a few pixels exceeding 775 kg $m^{-1}s^{-1}$. The results suggest increasing slopes for most of the AR types, with AR types 1, 2, and 6 showing statistically significant increasing trends in maximum IVT. AR types 3 and 4 indicate positive trends that fall above the $p < 0.05$ level.

The composite IVT fields for the six nodes modeled by the ARDT75 SOM are depicted in Figure 3c. The SOM suggests that increasing the IVT threshold to 750 kg $m^{-1}s^{-1}$ effectively removes zonally oriented ARs. The SOM organized the 488 ARs identified by ARDT75 into two clear Nor'easter nodes (nodes 5 and 6) while nodes 1–3 appear to be likely forced by strong mid-latitude cyclones transiting the northern portions of the study domain. The SOM also placed four ARs that were statistical outliers into node 4; due to the low number of events mapping to that AR type, the statistical properties of the Mann-Kendall test are irrelevant. Nodes 1 and 6 indicate increasing trends in the maximum IVT of these AR types, but neither achieve the significance threshold, partly due to the low counts of occurrence in some of the types. The composite IVT values of nodes 5 and 6 indicate peak IVT values that exceed 1,075 kg $m^{-1}s^{-1}$, making them the strongest nodes in the SOM.

ARDT5 and ARDT5-2 yield similar types of ARs, but ARDT5-2 has a higher composite IVT due to the higher IVT threshold used. Despite the ~80% reduction in ARs detected by ARDT5-2, the same spatial patterns of AR types are revealed. The reduction in sample size across the nodes in ARDT5-2 suggests that the trends revealed in maximum IVT are weakened slightly. In both ARDT5 and ARDT5-2, the primary Nor'easter nodes (node 1 for both ARDT5 and ARDT5-2 SOMs) show statistically significant increases in maximum IVT. Other similarities in patterns elucidated are the strong trends in ARs that have a southern origin in the Gulf of Mexico. In ARDT5, nodes 2, 4, and 6 all show statistically significant increases and have origins in the Gulf of Mexico while ARDT5-2 nodes 2 and 6 showing statistically significant increases (node 4 falls just outside the bounds of statistical significance).

When analyzing ARDT75, the statistical tests of maximum IVT reveal weaker trends (Figure 3c). This suggests a few possibilities. One possibility is that by excluding the lower end ARs included in ARDT5 and ARDT5-2, the higher-end events do not exhibit statistically significant increases in maximum IVT. The other potential is that the number of observed ARs matching to the nodes is small, and thus, meeting the statistical significance requirements are more difficult. The results in Section 3.6 will further explore the possibility of the lower to moderate ARs driving the statistical increases detected in ARDT5 and ARDT5-2. The lack of statistically significant trends in ARDT75 highlights the importance of threshold choice when conducting AR research.

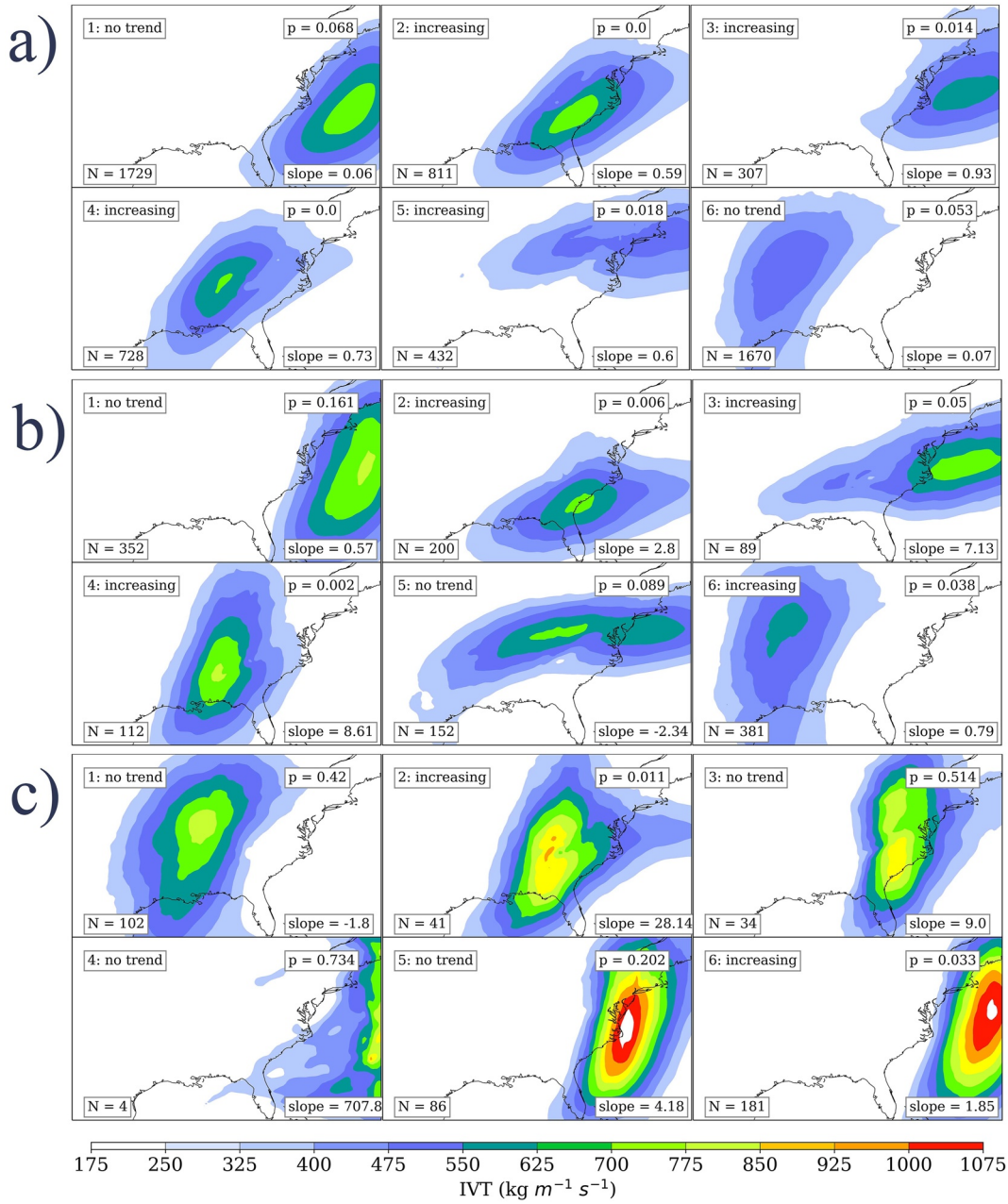

Figure 3. Composite integrated vapor transport (IVT) for each of the six atmospheric river (AR) types resolved by the (a) ARDT5 SOM, (b) ARDT5-2 SOM, and (c) ARDT75 SOM with the number of ARs mapping to each node (lower-left of each panel), Mann-Kendall derived slope of the trend in maximum IVT over the study period (lower-right), *p*-value from the Mann-Kendall test (upper-right), and the statistical significance of each trend (upper-left).

Figure 4 shows the distribution of maximum IVT by AR type which corresponds to nodes 1–6 of ARDT5-2 in Figure 3b. This helps visualize the variability and range of possible IVT by AR type. The most obvious finding of this analysis is how the upper end of the IVT maximum distribution is dominated by the Nor'easter node type (AR type 1). This is likely a result of these storms mobilizing the elevated IVT associated with the Gulf Stream (Figure 2). The lower end of the maximum IVT distribution tends to be dominated by node types 2, 3, and 5, partially due to weaker cyclogenesis and kinematic forcing. The wide distribution of IVT maximum, and partial dependence on AR type, illustrates the need to statistically evaluate trends in ARs by AR type, compared to analyzing trends in aggregate.

Additional Mann-Kendall tests determined if any statistically significant trends existed in the 41-year time series for each node (AR type). The metrics chosen (maximum IVT, mean IVT, and AR length) to represent the extent

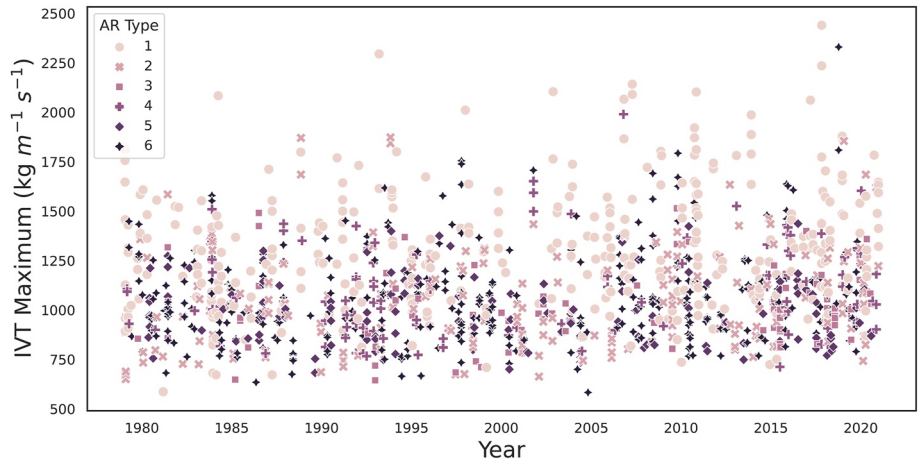

Figure 4. Integrated vapor transport maximum (i.e., 9-pixel mean) of all atmospheric rivers (ARs) detected by ARDT5-2 with color and shape denoting AR type from Figure 3b.

and magnitude of ARs follow recent literature in the research domain (e.g., Huang et al., 2020). The results of these tests are summarized in Table 2. Across all of the ARDT thresholds used, two themes are revealed. First, the Nor'easter nodes and the AR types that are connected to the Gulf of Mexico from ARDT5 and ARDT5-2 tend to have the strongest trends, despite the statistical metric. Second, as the IVT and/or length thresholds increase, the statistical significance of the trends decreases. This is likely due to the combination of smaller sample sizes where outlier data can influence the statistical tests and/or the possibility that many of the trends detected are being driven by the lower- or moderate- intensity ARs. The trends in ARDT75 are noisy and yield few statistically significant trends. However, two of the six AR types in ARDT75 indicate a statistically significant trend in the length of the ARs. This suggests a lengthening of the ARs in nodes 2 and 6. Node 2 is rooted in the Gulf of Mexico while node 6 is a Nor'easter-driven AR.

Table 2
Statistical Significance of Mann-Kendall Trends ($p < 0.05$) of AR Metrics for Each ARDT Type

Node number	AR IVT maximum	AR mean IVT	Number of pixels in AR (size)
ARDT5			
1*	Increasing	Increasing	—
2+	Increasing	Increasing	Increasing
3	Increasing	Increasing	Increasing
4+	Increasing	—	Increasing
5	—	Decreasing	Increasing
6+	Increasing	—	—
ARDT5-2			
1*	Increasing	Increasing	—
2+	Increasing	Increasing	Increasing
3	—	—	Increasing
4	—	—	Increasing
5+	—	—	—
6+	Increasing	—	Increasing
ARDT75			
1+	—	—	—
2+	—	—	Increasing
3+	—	—	—
4*	—	—	—
5*	—	—	—
6*	—	—	Increasing

Note. Superscript "+" indicates an AR type originating in the Gulf of Mexico while superscript "*" indicates a Nor'easter AR type.

3.3. Mean Sea-Level Pressure Composite Maps for ARDT 5-2

In subsequent subsections, the results focus on ARDT5-2. The ARs detected with ARDT5-2 yield similar AR types as ARDT5 and filter the shorter ARs that make up ~80% of the ARs detected by ARDT5. ARDT75 tends to be skewed to ARs driven by Nor'easters (247 of 488) and includes a node that only incorporates 4 ARs, suggesting there isn't enough variability to justify six nodes in the SOM.

In the preceding results, the most statistically significant outputs appear to be associated with Nor'easter-driven ARs as well as ARs driven by mid-latitude cyclogenesis where the warm conveyor belt originates over the Gulf of Mexico. These assumptions are vindicated in the analysis summarized in Figure 5. By comparing the results of Figure 5 with Figure 3b, node 1 is confirmed as a Nor'easter AR type as illustrated by the strong low-pressure situation over the Northeast US coastline, likely representing both Miller A and B type storms (Miller, 1946). In Figure 3b, the composite IVT is highest for node 1, which is physically consistent with the strongest kinematic forcing shown in node 1 of Figure 5. Nodes 4 and 6 represent mid-latitude cyclones, though the composite MSLP appears slightly weaker. These AR types are most likely representing a range of mid-latitude cyclones transiting the northern latitudes of the study domain, from the Central Great Plains to the Great Lakes Region. These cyclones position the origin of the warm

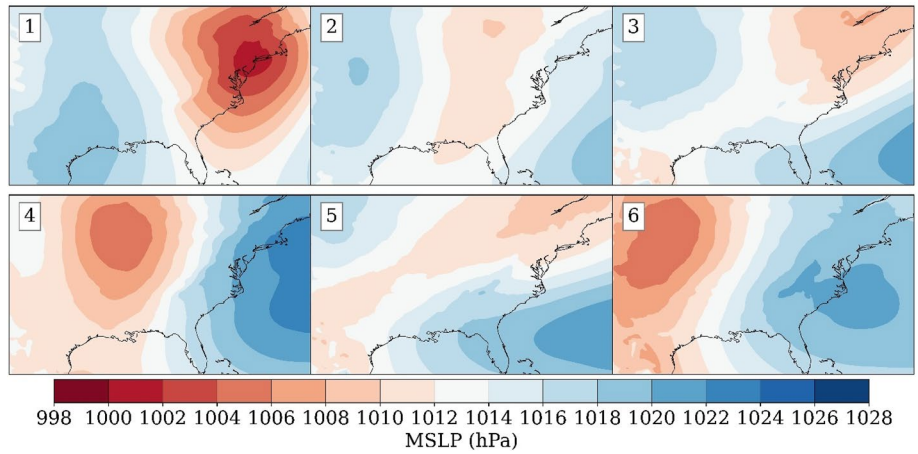

Figure 5. Composite MSLP for all atmospheric rivers (ARs) mapping to each AR type for the ARDT5-2 SOM.

conveyor belt and/or the low-level jet over the Gulf of Mexico–a common feature detected in previous AR literature (Lavers & Villarini, 2013; Moore et al., 2012; Ralph & Dettinger, 2011; Rutz et al., 2014).

Nodes 2, 3, and 5 of ARDT5-2 resolve ARs that stem from atmospheric conditions with less obvious kinematic forcing and lack the influence of strong cyclogenesis (Figure 5). This could be the result of ARs with greater spatial variability being grouped together in the node and/or they represent ARs that form from more benign physical forcings. As shown in Table 2, node 2 ARs exhibited statistically significant increasing trends in maximum IVT, mean IVT, and the AR length over the study period. Nodes 3 and 5 likely incorporate ARs that are detected due to strong background moisture and lower kinematic forcing, similar to those observed with stationary boundaries. This argument is strengthened due to the frequency of these node types during May–August (Figure 6b). The MSLP gradient observed in nodes 3 and 5 position the strongest gradients over the Gulf of Mexico and Gulf Stream. These gradients, and the potential air mass boundaries that may result, could be enough kinematic forcing to drive the IVT values above the 500 kg $m^{-1}s^{-1}$ threshold. This is informed by the exclusion of these AR types in the SOM for the 750 kg $m^{-1}s^{-1}$ in Figure 3c. Further evidence of the more limited kinematic forcing was provided in Figure 4 which shows that nodes 2, 5, and 6 tend to produce ARs on the lower-end of the maximum IVT distribution for ARDT5-2.

3.4. Temporal Characteristics of AR Types

To comprehensively understand the AR types revealed, particularly of ARDT5-2, the temporal characteristics of each AR type were investigated. In particular, the yearly counts of each AR type are summarized in Figure 6a and the monthly counts are illustrated in Figure 6b. While Figure 6a highlights the interannual variability of the AR types, a couple of interesting findings are revealed. In the last decade, occurrence of AR types 1–3 and 6 tend to reach their peaks. AR types 4 and 5 have peaks in their occurrence over the last decade, but are preceded by similar peaks in the 1980s and 1990s. 2010 shows a maximum in counts in both AR types 1 and 6. Future studies will address this 2010 peak in ARs and possible linkages to climatic variability (e.g., ENSO, NAO, MJO) during this period (e.g., Guirguis et al., 2019; S. Kim & Chiang, 2022; W. Kim et al., 2011).

Figure 6b highlights the seasonality of the AR types in ARDT5-2. It provides further evidence that node 1 is primarily Nor'easter driven due to the peak in AR counts in the cold season with very few detected in May–August. Node 2 exhibits a similar distribution, although with fewer events. This suggests that node 2 may capture some weaker Nor'easter type events, in addition to stationary boundaries, as posited in Section 3.3. Nodes 3 and 5 show similar distributions, with peaks occurring in the warm season, providing strengthened evidence that these AR types are likely the result of elevated background moisture and lower kinematic forcing. Node 4 peaks in the early cold season with lower counts persisting until June-September when these AR types are virtually non-existent in the climatology. Lastly, node 6 exhibits a bi-modal distribution with peaks in the late Spring and Fall. This node also reaches a minimum in the winter months with a second minima in late summer. This highlights the non-linearity in AR detection, driven by the multivariate IVT calculation. Node 6 is likely responding

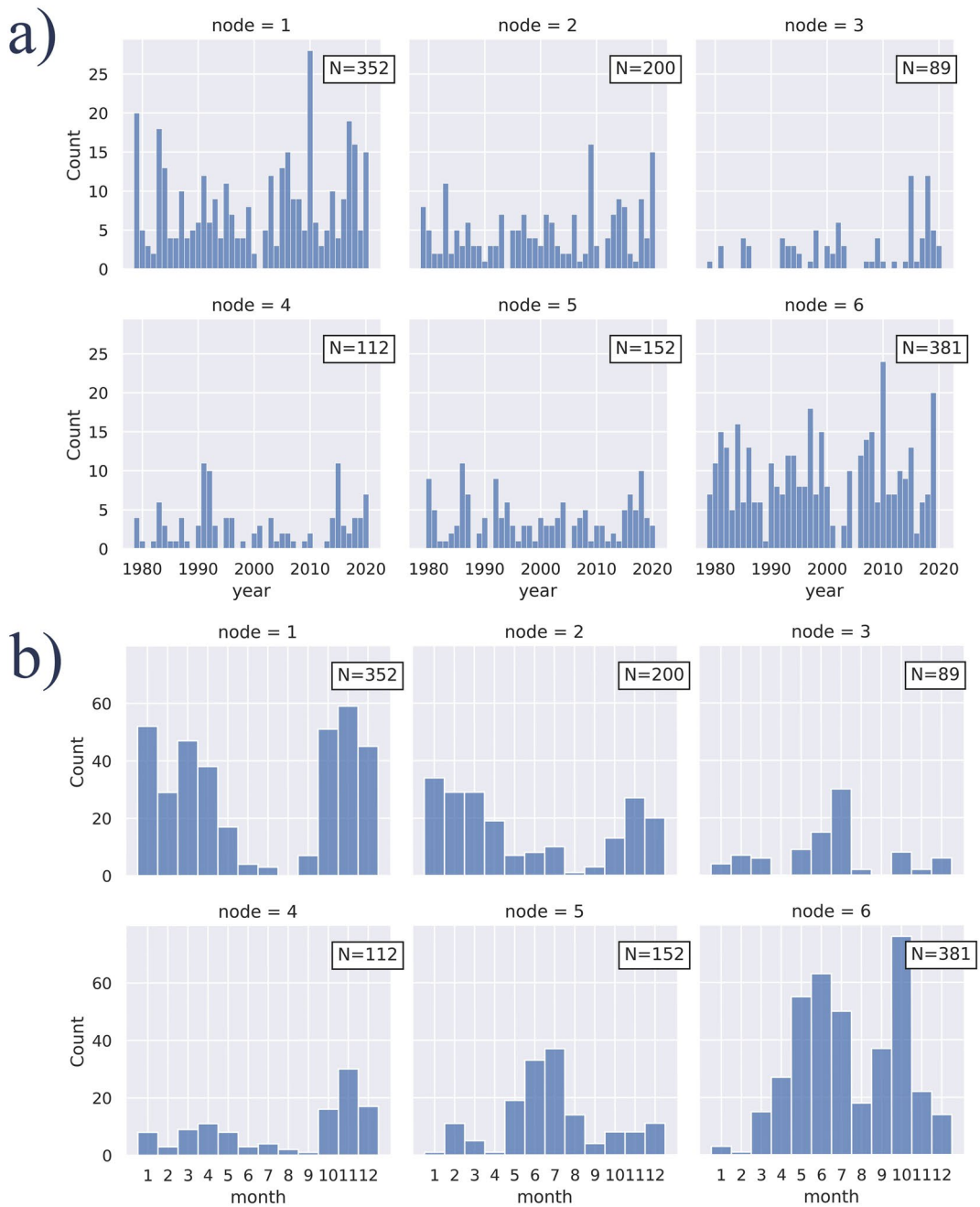

Figure 6. (a) Annual and (b) monthly counts of each atmospheric river type of the ARDT5-2 SOM.

in the winter to limited moisture supply in the winter as the western Gulf of Mexico cools to its minimum, making it difficult to meet the IVT threshold, while the second minima in summer is likely responding to the limited kinematic forcing due to decreased cyclogenesis.

3.5. AR Types and Precipitation

PRISM data were aggregated to produce a mean state of daily precipitation for each node type in the ARDT5-2 SOM. Using the input vectors (i.e., IVT for each 6-hr period) that mapped to each node, the mean for the PRISM data was acquired (Figure 7a). Since PRISM data are only available at daily temporal resolution, the PRISM data for the day in which each AR occurred was used. Previous research has shown that stronger ARs are

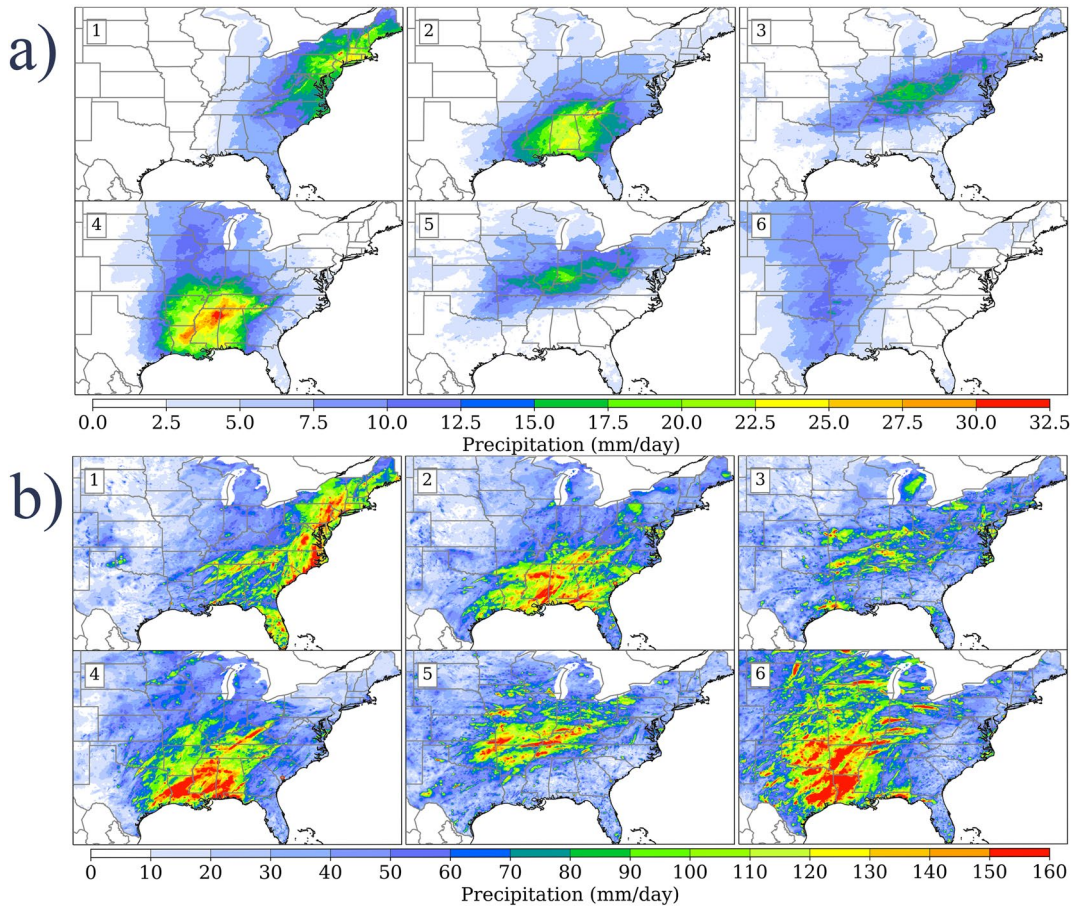

Figure 7. (a) Composite PRISM daily precipitation (mm/day) maps for each node type for the ARDT5-2 SOM. (b) PRISM pixel daily maximum precipitation (mm/day) maps for each node type for the ARDT5-2 SOM.

associated with increased precipitation efficiency (e.g., Lamjiri et al., 2017; Lavers & Villarini, 2013; Nayak & Villarini, 2018; Sharma & Déry, 2020). This analysis helps to understand if the ARs produce coherent spatial patterns that could be helpful for relating AR type to areas of increased risk for AR-driven flooding.

Nodes 1, 2, and 4 produce the most spatially coherent precipitation patterns (Figure 7a). These three ARs are clearly rooted in the Gulf of Mexico and/or Gulf Stream and tend to produce the strongest mean-state precipitation patterns. These three nodes also show some topographic forcing in the composite precipitation (Figure 1b). Node 1 shows topographic enhancement along the Central and Northern Appalachian Mountain range. Meanwhile, nodes 2 and 4 suggest some topographic enhancement of AR driven precipitation along the Southern Appalachian Mountains. This would be similar to many studies that have demonstrated a similar effect on the US West Coast (e.g., Payne et al., 2020; Ralph et al., 2018). When relating these results back to the Mann-Kendall tests in Table 2, ARDT5-2 nodes 1, 2, and 4 all exhibited some statistically significant trends in AR properties. In additional to topographic enhancement, these precipitation patterns highlight urban areas that are prone to AR-driven, heavy precipitation. The Nor'easter node (e.g., node 1) shows enhanced precipitation along the Northeast Corridor from Washington, D.C. to Boston, MA. This is consistent with earlier research showing increases in extreme precipitation in the Northeast US (Agel et al., 2018; Collow et al., 2016). Nodes 2 and 4 drive heavy precipitation in the Tennessee River Valley and Deep South, impacting metropolitan areas like Nashville, TN and Atlanta, GA.

Interestingly, three of the nodes (3, 5, and 6) in the ARDT5-2 SOM show little coherent spatial patterns of heavy precipitation. This higher spatial variability in precipitation pattern suggests lack of consistency within the node in terms of precipitation forcing. Node 6, in particular, shows practically no composite pixels with more than 10 mm of rainfall (Figure 7a). To a lesser extent, this is similar to what is likely occurring in nodes 3 and 5. It's

important to note, this does not mean these AR types cannot produce heavy rainfall, but, in composite, they tend to have less spatial cohesiveness in terms of precipitation.

To further illustrate this point, Figure 7b is presented to highlight the maximum rainfall at each grid point for each AR type. The colormap used in this figure is different than 7a, where the maximum contour level now represents daily rainfall >160 mm (~7 inches). This highlights that all of these AR types, excluding node 3, are capable of producing potentially catastrophic rainfall at discrete locations. In particular, this helps highlight node 6 and the precipitation that it can produce. In Figure 7a, node 6 shows no spatial cohesiveness, but Figure 7b highlights that individual ARs in this broader AR type are capable of producing areas of extreme rainfall.

3.6. Nested SOMs

The inclusion of a nested SOM methodology allows for analysis of the variability within each node type and to assess the potential sources of trends. In other words, are there certain categories of ARs driving the statistical significance? Nested SOMs were built for nodes 1, 2, and 6 for the ARDT5-2 SOM, as these nodes exhibited at least two AR statistics with significant increases (statistically significant increases in maximum IVT was present for all three).

The nested SOM for node 1 highlights the variability within node 1 of ARDT5-2 (Figure 8). For reference, this is a SOM showing the variability within AR type 1 in Figure 3b. It provides the opportunity to evaluate which of the Nor'easter type ARs may be driving the statistically significant increases denoted in Table 2. Figure 8a shows the patterns revealed with several intense, landfalling ARs indicated in nodes 1, 2, and 4. All three AR types exhibit increasing trends in maximum IVT with node 4 being statistically significant. It should also be noted that node 1 has a p-value of 0.052, just outside the threshold of statistical significance. Node 6, which shows ARs as they propagate out of the study domain, is also a land-falling AR in the Canadian Maritimes and has a positive slope with a p-value just outside of the bounds used in this study. Nodes 3 and 5, both of which are weaker non-land-falling AR types, have the weakest trends. This exercise provides evidence that the statistical significance of node 1 of the ARDT5-2 SOM is being primarily driven by strong, land-falling ARs perpetuated by Nor'easters, as opposed to offshore Nor'easters.

Figure 8b shows the results of the nested SOM for node 6 in the ARDT5-2 SOM. The results here suggest nodes 2, 5, and 6 exhibit the strongest positive increases (while 5 of the 6 all exhibit increasing trends). However, only node 2 is statistically significant with 5 and 6 falling just outside the of the p-value threshold. These three nodes all represent some of the stronger ARs.

Figure 8c illustrates the nested SOM from node 2 in the ARDT5-2 SOM where several similar AR types are revealed, particularly the spatial positioning of the AR in nodes 1–5. The nested SOM has organized the data by differing magnitudes of IVT, where nodes 1 and 5 are the weakest ARs and nodes 2–4 represent moderate ARs. Interestingly, node 6 seems to represent ARs associated with mid-latitude cyclones transiting the Great Lakes region. This likely represents some outlier events that positioned the core of the AR over the Southeast Atlantic coastline and were captured in this type as a result. Much different than the other nested SOMs, Figure 8c shows that one of the weakest AR types is the statistically significant subtype, likely driving the statistical significance of node 2 in the ARDT5-2 SOM.

4. Discussion

By analyzing ARs with multiple ARDT thresholds, this study examines ARs while simultaneously considering the influence of ARDT threshold selection on the results. This provides increased confidence in the results and offers guidance on which ARDT criteria can/should be used for certain analyses. By modeling the ARs produced by three different ARDT criteria with SOMs and then statistically analyzing the properties of the AR types, any trends can be compared against other results to ensure that outcomes are not the result of model selection and/or the specific AR samples. Some trends detected were consistent across more than one SOM.

In particular, AR types that were driven primarily by mid-latitude cyclones, such as Nor'easters, tended to show consistent increasing trends in IVT and length across ARDT5 and ARDT5-2, strengthening the results and findings. Qualitatively speaking, the types of ARs derived using the different criteria indicate that using stricter conditions tends to result in more meridional wind forcing, and less zonal wind forcing, as suggested by the axis of maximum moisture transport (Figure 3).

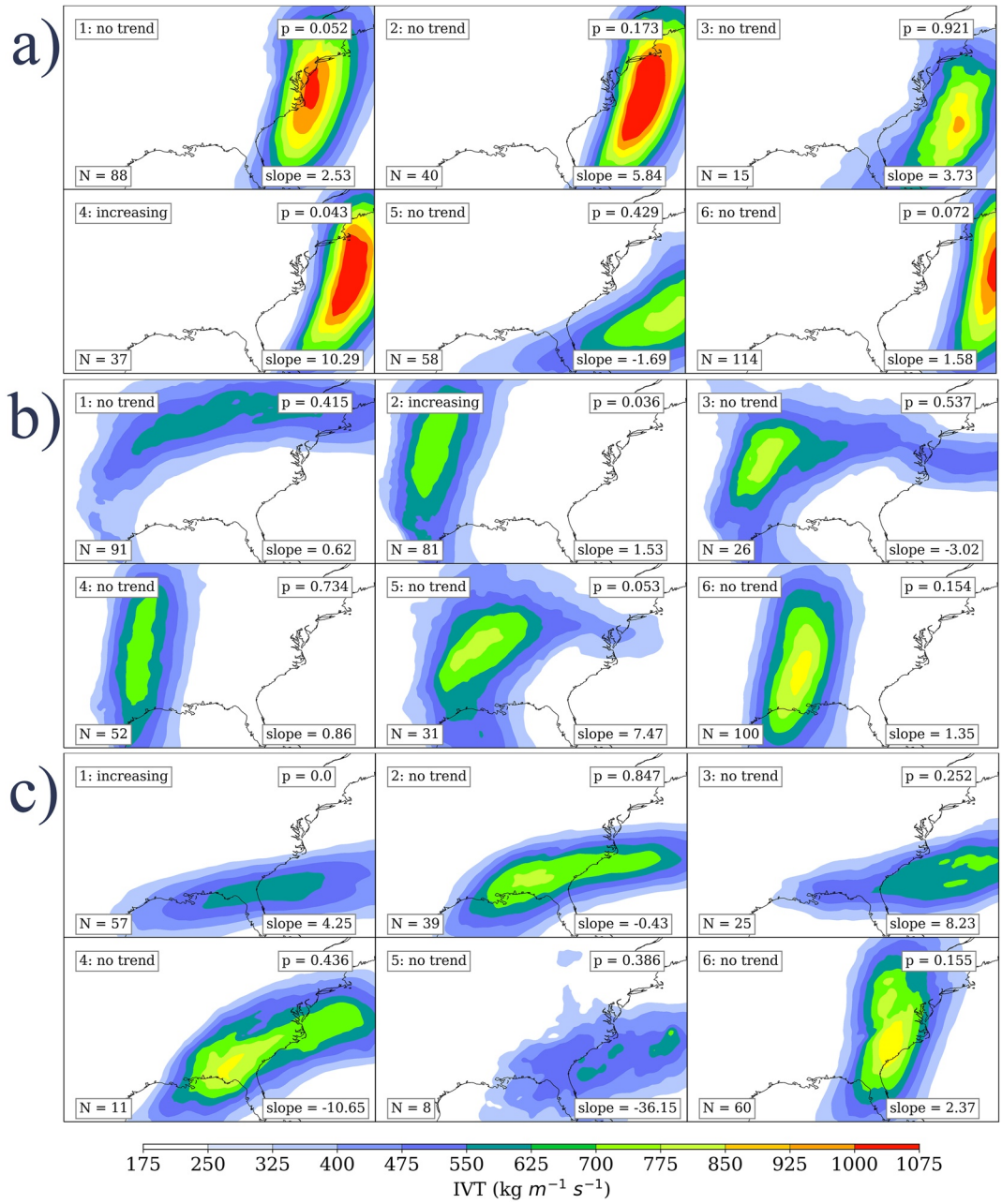

Figure 8. Composite integrated vapor transport (IVT) for each of the six atmospheric river (AR) types resolved by the nested SOM from (a) node 1, (b) node 6, and (c) node 2 of the ARDT5-2 SOM in Figure 3b. The number of ARs mapping to each node (lower-left of each panel), Mann-Kendall derived slope of the trend in maximum IVT over the study period (lower-right), *p*-value from the Mann-Kendall test (upper-right), and the statistical significance of each trend (upper-left).

Mid-latitude cyclones produce some of the highest impact weather events that affect CONUS east of the Rockies and have been identified as the primary drivers of ARs in the literature (Dirmeyer & Kinter, 2009; Lavers & Villarini, 2013; Mestas-Nuñez et al., 2007; D. K. Miller et al., 2019; Moore et al., 2012; Villarini, 2016). ARs have been of great interest in the climate literature over the last 20 years, due to their linkages to extreme precipitation events, and associated landscape impacts (Biasutti et al., 2016; Cordeira et al., 2019; Corringham et al., 2019; Eiras-Barca et al., 2016; J. Kim et al., 2013; Leung & Qian, 2009; Neiman et al., 2011; Pasquier et al., 2019; Stanley et al., 2020). The results presented here, suggest that the AR types most associated with strong extratropical cyclones show indications of statistically significant increases in AR strength and/or size, particularly Nor'easters.

The most consistent statistically significant results tend to be associated with ARs forced by strong, extratropical cyclones positioned with the strongest moisture flux (e.g., AR core) situated over the Gulf Stream. In particular, Figure 8a shows that within the Nor'easter AR type, the strong, landfalling ARs are driving much of the statistically significant increases detected. These high-impact AR types are likely increasing in strength and/or length due to increased moisture uptake from the Gulf Stream.

One potential driver of the recent increase in IVT, particularly to the strong nor'easter AR types, is the observed increasing sea surface temperatures (SSTs) (Bulgin et al., 2020; Karnauskas et al., 2021; X.-Y. Wu et al., 2020). These increases in SSTs during the study period along the Gulf Stream and off the coast of the Northeast US are related to climate change and the potential slowing of the Atlantic Meridional Overturning Circulation (AMOC) (Frajka-Williams et al., 2019; Smeed et al., 2014, 2018). In a warming climate, landfalling ARs are expected to increase in frequency and intensity due to the increase in IVT that alludes to an increase in moisture transport as temperatures rise (Algarra et al., 2020). As reliable observation and satellite datasets cover increasingly longer temporal ranges, the trends elucidated in the reanalysis data in this study should be further investigated using independent datasets to rule out any trends being a function of the data assimilation scheme employed by the reanalysis model.

The impact of increasing moisture transport could be significant across the northeast corridor from Washington D.C. to Coastal Maine, as it increases the risk of extreme precipitation from landfalling ARs. Additionally, node 2 in ARDT5-2 represents low pressure systems situated over the Great Lakes region, positioning the highest IVT over the Southeast US and Tennessee River Valley. This setup exposes cities such as Nashville and Atlanta to extreme rainfall potential. Shown in Figure 8, a localized maximum in rainfall is situated near the Nashville metropolitan area–a synoptic regime that becomes increasingly costly with occurrence. The results presented here imply this type of AR has been increasing in length over the 41-year time series. Similar node types in ARDT5 and ARDT75 also indicate increasing trends in length of these types of ARs. Nashville, in particular, has already faced documented significant flooding from an AR driven by a low pressure situated over the Upper Midwest (Moore et al., 2012).

This study also provides evidence that the AR types that transit the Appalachian Mountain range result in higher precipitation, suggesting that topography assists in increasing precipitation efficiency in this study domain. This finding is consistent with studies on the U.S West Coast (Cordeira et al., 2019; Payne et al., 2020).

5. Conclusions

The AR literature has grown rapidly over the last 20 years, with most of the focus on the West Coast US where AR-induced extreme precipitation events are commonplace. As the AR literature has expanded, so has the spatial domain of interest. The results presented here provide new insight into the trends in moisture transport and the specific AR types driving increases in AR magnitude and strength. This study also highlights the precipitation patterns produced by all existing AR types across the study domain. Through this, it is revealed that topography helps to lead to localized extremes in AR-driven precipitation.

The analysis examines all months but shows that many of the warm season ARs do not produce spatially consistent precipitation patterns, largely due to the lack of kinematic forcing from a strong cyclone. The warm season ARs are likely meeting the AR thresholds due to enhanced background moisture and minimal advection (i.e., wind speeds are low). However, many of the AR types during the cold season produce robust precipitation patterns that are spatially consistent. These ARs tend to be driven by extratropical cyclones. This suggests that, while warm seasons may have environments of enhanced background moisture that meet these AR thresholds, they do not ultimately manifest in spatially consistent precipitation patterns. Thus, in the cold season, extratropical driven AR types are most efficient at producing precipitation. Additionally, this study indicates that the AR types that interact with the mountainous terrain associated with the Appalachian Mountain range produce the most intense precipitation, similar to AR interactions with terrain on the West Coast of the United States and Europe. Training multiple SOMs allows for an examination of consilience of results and provides strengthened evidence of potential trends in IVT for different AR types.

The results indicate most ARs in the study domain are forced by extratropical cyclones, with lee side low pressure systems and coastal lows along the Atlantic Coast (e.g., nor'easters) responsible for producing the strongest ARs. Mann-Kendall trend analyses indicate increasing trends in IVT and the length of some AR types. The most

consistent statistically significant increasing trends are for ARs associated with mature cyclones in the Upper Midwest/Great Lakes regions, which position the most intense IVT over the southeast US and Tennessee River Valley, and are rooted in the Gulf of Mexico. Trends are also consistent with coastal cyclones over the northeast US with the most intense IVT transiting the Mid-Atlantic and Northeast US Recent studies have found similar increasing trends for IVT and moisture transport in the study domain which can feedback on the AR metrics associated with some Nor'easter forced ARs (Teale & Robinson, 2022; Y. Wu et al., 2020).

Future studies are necessary to further explore the trends suggested by the ARDT criteria utilized in this study. This research provides some potential future research objectives to the discipline by identifying the types of ARs that produce heavy rainfall in the metropolitan areas of the Eastern US and the Appalachian Mountains and the statistically significant trends associated with them. These AR types, due to their societal relevance, should be investigated further to see if additional intensification and elongation are documented in GCMs run for future climate change scenarios. Additionally–as has been conducted in other study regimes–sources of climate variability (e.g., ENSO, MJO) should be explored to determine their potential influence on the strength and frequency of ARs (Guirguis et al., 2019; S. Kim & Chiang, 2022).

Data Availability Statement

In keeping with the FAIR data project guidelines from the editorial board of the Journal of Geophysical Research-Atmospheres, the primary data created for this project are available publicly at the Virginia Tech Data Repository located at https://data.lib.vt.edu/ (Ramseyer, 2021, https://doi.org/10.7294/15125586.v1).

Acknowledgments
The authors extend gratitude to the anonymous reviewers of this manuscript for their thorough and exhaustive reviews, which significantly improved the quality of the research. The authors also thank the European Centre for Medium-Range Weather Forecasts for making the ERA5 reanalysis data open-access.

References

Agel, L., Barlow, M., Feldstein, S. B., & Gutowski, W. J. (2018). Identification of large-scale meteorological patterns associated with extreme precipitation in the US northeast. *Climate Dynamics*, *50*(5), 1819–1839. https://doi.org/10.1007/s00382-017-3724-8

Algarra, I., Nieto, R., Ramos, A. M., Eiras-Barca, J., Trigo, R. M., & Gimeno, L. (2020). Significant increase of global anomalous moisture uptake feeding landfalling Atmospheric Rivers. *Nature Communications*, *11*(1), 5082. https://doi.org/10.1038/s41467-020-18876-w

Biasutti, M., Seager, R., & Kirschbaum, D. B. (2016). Landslides in West Coast metropolitan areas: The role of extreme weather events. *Weather and Climate Extremes*, *14*, 67–79. https://doi.org/10.1016/j.wace.2016.11.004

Brands, S., Gutiérrez, J. M., & San-Martín, D. (2017). Twentieth-century atmospheric river activity along the west coasts of Europe and North America: Algorithm formulation, reanalysis uncertainty and links to atmospheric circulation patterns. *Climate Dynamics*, *48*(9), 2771–2795. https://doi.org/10.1007/s00382-016-3095-6

Bulgin, C. E., Merchant, C. J., & Ferreira, D. (2020). Tendencies, variability and persistence of sea surface temperature anomalies. *Scientific Reports*, *10*(1), 7986. https://doi.org/10.1038/s41598-020-64785-9

Cassano, E., Glisan, J., Cassano, J., Gutowski, W., & Seefeldt, M. (2015). Self-organizing map analysis of widespread temperature extremes in Alaska and Canada. *Climate Research*, *62*(3), 199–218. https://doi.org/10.3354/cr01274

Chen, X., Leung, L. R., Gao, Y., Liu, Y., Wigmosta, M., & Richmond, M. (2018). Predictability of extreme precipitation in western U.S. watersheds based on atmospheric river occurrence, intensity, and duration. *Geophysical Research Letters*, *45*(21), 11693–11701. https://doi.org/10.1029/2018GL079831

Collow, A. B. M., Bosilovich, M. G., & Koster, R. D. (2016). Large-scale influences on summertime extreme precipitation in the northeastern United States. *Journal of Hydrometeorology*, *17*(12), 3045–3061. https://doi.org/10.1175/JHM-D-16-0091.1

Collow, A. B. M., Shields, C. A., Guan, B., Kim, S., Lora, J. M., McClenny, E. E., et al. (2022). An overview of ARTMIP's tier 2 reanalysis Intercomparison: Uncertainty in the detection of atmospheric rivers and their associated precipitation. *Journal of Geophysical Research: Atmospheres*, *127*(8), e2021JD036155. https://doi.org/10.1029/2021JD036155

Cordeira, J. M., Stock, J., Dettinger, M. D., Young, A. M., Kalansky, J. F., & Ralph, F. M. (2019). A 142-year climatology of northern California landslides and atmospheric rivers. *Bulletin of the American Meteorological Society*, *100*(8), 1499–1509. https://doi.org/10.1175/BAMS-D-18-0158.1

Corringham, T. W., Ralph, F. M., Gershunov, A., Cayan, D. R., & Talbot, C. A. (2019). Atmospheric rivers drive flood damages in the western United States. *Science Advances*, *5*(12), eaax4631. https://doi.org/10.1126/sciadv.aax4631

Dacre, H. F., Clark, P. A., Martinez-Alvarado, O., Stringer, M. A., & Lavers, D. A. (2015). How do atmospheric rivers form? *Bulletin of the American Meteorological Society*, *96*(8), 1243–1255. https://doi.org/10.1175/BAMS-D-14-00031.1

Dacre, H. F., Martínez-Alvarado, O., & Mbengue, C. O. (2019). Linking atmospheric rivers and warm conveyor belt airflows. *Journal of Hydrometeorology*, *20*(6), 1183–1196. https://doi.org/10.1175/JHM-D-18-0175.1

Daly, C., Doggett, M. K., Smith, J. I., Olson, K. V., Halbleib, M. D., Dimcovic, Z., et al. (2021). Challenges in observation-based mapping of daily precipitation across the conterminous United States. *Journal of Atmospheric and Oceanic Technology*, *38*(11), 1979–1992. https://doi.org/10.1175/JTECH-D-21-0054.1

Debbage, N., Miller, P., Poore, S., Morano, K., Mote, T., & Shepherd, J. M. (2017). A climatology of atmospheric river interactions with the southeastern United States coastline. *International Journal of Climatology*, *37*(11), 4077–4091. https://doi.org/10.1002/joc.5000

Dee, D. P., Uppala, S. M., Simmons, A. J., Berrisford, P., Poli, P., Kobayashi, S., et al. (2011). The ERA-interim reanalysis: Configuration and performance of the data assimilation system. *Quarterly Journal of the Royal Meteorological Society*, *137*(656), 553–597. https://doi.org/10.1002/qj.828

Dettinger, M. D., Ralph, F. M., Das, T., Neiman, P. J., & Cayan, D. R. (2011). Atmospheric rivers, floods and the water resources of California. *Water*, *3*(2), 445–478. https://doi.org/10.3390/w3020445

Dirmeyer, P. A., & Kinter, J. L. (2009). The "Maya Express": Floods in the U.S. Midwest. *Eos, Transactions American Geophysical Union*, *90*(12), 101–102. https://doi.org/10.1029/2009EO120001

Dirmeyer, P. A., & Kinter, J. L. (2010). Floods over the U.S. Midwest: A regional water cycle perspective. *Journal of Hydrometeorology*, *11*(5), 1172–1181. https://doi.org/10.1175/2010JHM1196.1

Edwards, T. K., Smith, L. M., & Stechmann, S. N. (2020). Atmospheric rivers and water fluxes in precipitating quasi-geostrophic turbulence. *Quarterly Journal of the Royal Meteorological Society*, *146*(729), 1960–1975. https://doi.org/10.1002/qj.3777

Eiras-Barca, J., Brands, S., & Miguez-Macho, G. (2016). Seasonal variations in North Atlantic atmospheric river activity and associations with anomalous precipitation over the Iberian Atlantic Margin. *Journal of Geophysical Research: Atmospheres*, *121*(2), 931–948. https://doi.org/10.1002/2015JD023379

Ford, T. W., Rapp, A. D., & Quiring, S. M. (2015). Does afternoon precipitation occur preferentially over dry or wet soils in Oklahoma? *Journal of Hydrometeorology*, *16*(2), 874–888. https://doi.org/10.1175/JHM-D-14-0005.1

Frajka-Williams, E., Ansorge, I. J., Baehr, J., Bryden, H. L., Chidichimo, M. P., Cunningham, S. A., et al. (2019). Atlantic meridional overturning circulation: Observed transport and variability. *Frontiers in Marine Science*, *0*. https://doi.org/10.3389/fmars.2019.00260

Gershunov, A., Shulgina, T., Ralph, F. M., Lavers, D. A., & Rutz, J. J. (2017). Assessing the climate-scale variability of atmospheric rivers affecting western North America. *Geophysical Research Letters*, *44*(15), 7900–7908. https://doi.org/10.1002/2017GL074175

Guan, B., & Waliser, D. E. (2015). Detection of atmospheric rivers: Evaluation and application of an algorithm for global studies. *Journal of Geophysical Research: Atmospheres*, *120*(24), 12514–12535. https://doi.org/10.1002/2015JD024257

Guirguis, K., Gershunov, A., Shulgina, T., Clemesha, R. E. S., & Ralph, F. M. (2019). Atmospheric rivers impacting Northern California and their modulation by a variable climate. *Climate Dynamics*, *52*(11), 6569–6583. https://doi.org/10.1007/s00382-018-4532-5

Hersbach, H., Bell, B., Berrisford, P., Hirahara, S., Horányi, A., Muñoz-Sabater, J., et al. (2020). The ERA5 global reanalysis. *Quarterly Journal of the Royal Meteorological Society*, *146*(730), 1999–2049. https://doi.org/10.1002/qj.3803

Hewitson, B. C., & Crane, R. G. (2002). Self-organizing maps: Applications to synoptic climatology. *Climate Research*, *22*(1), 13–26. https://doi.org/10.3354/cr022013

Higgins, R. W., Kousky, V. E., & Xie, P. (2011). Extreme precipitation events in the south-central United States during may and June 2010: Historical perspective, role of ENSO, and trends. *Journal of Hydrometeorology*, *12*(5), 1056–1070. https://doi.org/10.1175/JHM-D-10-05039.1

Hirota, N., Takayabu, Y. N., Kato, M., & Arakane, S. (2016). Roles of an atmospheric river and a cutoff low in the extreme precipitation event in Hiroshima on 19 August 2014. *Monthly Weather Review*, *144*(3), 1145–1160. https://doi.org/10.1175/MWR-D-15-0299.1

Huang, X., Swain, D. L., & Hall, A. D. (2020). Future precipitation increase from very high resolution ensemble downscaling of extreme atmospheric river storms in California. *Science Advances*, *6*(29), eaba1323. https://doi.org/10.1126/sciadv.aba1323

Inda-Díaz, H. A., O'Brien, T. A., Zhou, Y., & Collins, W. D. (2021). Constraining and characterizing the size of atmospheric rivers: A perspective independent from the detection algorithm. *Journal of Geophysical Research: Atmospheres*, *126*(16), e2020JD033746. https://doi.org/10.1029/2020JD033746

Karnauskas, K. B., Zhang, L., & Amaya, D. J. (2021). The atmospheric response to North Atlantic SST trends, 1870–2019. *Geophysical Research Letters*, *48*(2), e2020GL090677. https://doi.org/10.1029/2020GL090677

Kashinath, K., Kashinath, K., Mudigonda, M., Kim, S., Kapp-Schwoerer, L., Graubner, A., et al. (2021). ClimateNet: An expert-labeled open dataset and deep learning architecture for enabling high-precision analyses of extreme weather. *Geoscientific Model Development*, *14*(1), 107–124. https://doi.org/10.5194/gmd-14-107-2021

Kendall, M. G. (1948). *Rank correlation methods*. Griffin.

Kim, J., Waliser, D. E., Neiman, P. J., Guan, B., Ryoo, J., & Wick, G. A. (2013). Effects of atmospheric river landfalls on the cold season precipitation in California. *Climate Dynamics*, *40*(1–2), 465–474. https://doi.org/10.1007/s00382-012-1322-3

Kim, S., & Chiang, J. C. H. (2022). Atmospheric river lifecycle characteristics shaped by synoptic conditions at genesis. *International Journal of Climatology*, *42*(1), 521–538. https://doi.org/10.1002/joc.7258

Kim, W., Yeh, S.-W., Kim, J.-H., Kug, J.-S., & Kwon, M. (2011). The unique 2009–2010 El Niño event: A fast phase transition of warm pool El Niño to La Niña. *Geophysical Research Letters*, *38*(15), L15809. https://doi.org/10.1029/2011GL048521

Kirien, W., Jana, S., Schaller, N., & Rein, H. (2020). Future changes in atmospheric rivers and extreme precipitation in Norway. *Climate Dynamics*, *54*(3–4), 2071–2084. https://doi.org/10.1007/s00382-019-05099-z

Lamjiri, M. A., Dettinger, M. D., Ralph, F. M., & Guan, B. (2017). Hourly storm characteristics along the U.S. West Coast: Role of atmospheric rivers in extreme precipitation. *Geophysical Research Letters*, *44*(13), 7020–7028. https://doi.org/10.1002/2017GL074193

Landsea, C. W., & Franklin, J. L. (2013). Atlantic hurricane database uncertainty and presentation of a new database format. *Monthly Weather Review*, *141*(10), 3576–3592. https://doi.org/10.1175/MWR-D-12-00254.1

Lavers, D. A., & Villarini, G. (2013). Atmospheric rivers and flooding over the central United States. *Journal of Climate*, *26*(20), 7829–7836. https://doi.org/10.1175/JCLI-D-13-00212.1

Lavers, D. A., & Villarini, G. (2015). The contribution of atmospheric rivers to precipitation in Europe and the United States. *Journal of Hydrology*, *522*, 382–390. https://doi.org/10.1016/j.jhydrol.2014.12.010

Lavers, D. A., Villarini, G., Allan, R. P., Wood, E. F., & Wade, A. J. (2012). The detection of atmospheric rivers in atmospheric reanalyses and their links to British winter floods and the large-scale climatic circulation. *Journal of Geophysical Research*, *117*(D20), D20106. https://doi.org/10.1029/2012JD018027

Leung, L. R., & Qian, Y. (2009). Atmospheric rivers induced heavy precipitation and flooding in the western U.S. simulated by the WRF regional climate model. *Geophysical Research Letters*, *36*(3), L03820. https://doi.org/10.1029/2008GL036445

Lora, J. M., Mitchell, J. L., Risi, C., & Tripati, A. E. (2017). North Pacific atmospheric rivers and their influence on western North America at the Last Glacial Maximum. *Geophysical Research Letters*, *44*(2), 1051–1059. https://doi.org/10.1002/2016GL071541

Lora, J. M., Shields, C. A., & Rutz, J. J. (2020). Consensus and disagreement in atmospheric river detection: ARTMIP global catalogues. *Geophysical Research Letters*, *47*(20), e2020GL089302. https://doi.org/10.1029/2020GL089302

Mahoney, K., Jackson, D. L., Neiman, P., Hughes, M., Darby, L., Wick, G., et al. (2016). Understanding the role of atmospheric rivers in heavy precipitation in the southeast United States. *Monthly Weather Review*, *144*(4), 1617–1632. https://doi.org/10.1175/MWR-D-15-0279.1

Mann, H. B. (1945). Nonparametric tests against trend. *Econometrica*, *13*(3), 245–259. https://doi.org/10.2307/1907187

Mattingly, K. S., Ramseyer, C. A., Rosen, J. J., Mote, T. L., & Muthyala, R. (2016). Increasing water vapor transport to the Greenland Ice Sheet revealed using self-organizing maps: Increasing Greenland moisture transport. *Geophysical Research Letters*, *43*(17), 9250–9258. https://doi.org/10.1002/2016GL070424

Mestas-Nuñez, A. M., Enfield, D. B., & Zhang, C. (2007). Water vapor fluxes over the Intra-Americas Sea: Seasonal and interannual variability and associations with rainfall. *Journal of Climate*, *20*(9), 1910–1922. https://doi.org/10.1175/JCLI4096.1

Miller, D. K., Miniat, C. F., Wooten, R. M., & Barros, A. P. (2019). An expanded investigation of atmospheric rivers in the southern Appalachian Mountains and their connection to landslides. *Atmosphere*, *10*(2), 71. https://doi.org/10.3390/atmos10020071

Miller, J. E. (1946). Cyclogenesis in the Atlantic coastal region of the United States. *Journal of the Atmospheric Sciences*, *3*(2), 31–44. https://doi.org/10.1175/1520-0469(1946)003<0031:citacr>2.0.co;2

Mo, R., & Lin, H. (2019). Tropical–mid-latitude interactions: Case study of an inland-penetrating atmospheric river during a major winter storm over North America. *Atmosphere-Ocean*, *57*(3), 208–232. https://doi.org/10.1080/07055900.2019.1617673

Mo, R., So, R., Brugman, M. M., Mooney, C., Liu, A. Q., Jakob, M., et al. (2021). Column relative humidity and primary condensation rate as two useful supplements to atmospheric river analysis. *Water Resources Research*, *57*(11), e2021WR029678. https://doi.org/10.1029/2021WR029678

Moore, B. J., Neiman, P. J., Ralph, F. M., & Barthold, F. E. (2012). Physical processes associated with heavy flooding rainfall in Nashville, Tennessee, and vicinity during 1–2 May 2010: The role of an atmospheric river and mesoscale convective systems. *Monthly Weather Review*, *140*(2), 358–378. https://doi.org/10.1175/MWR-D-11-00126.1

Morioka, Y., Tozuka, T., & Yamagata, T. (2010). Climate variability in the southern Indian Ocean as revealed by self-organizing maps. *Climate Dynamics*, *35*(6), 1059–1072. https://doi.org/10.1007/s00382-010-0843-x

Nayak, M. A., & Villarini, G. (2017). A long-term perspective of the hydroclimatological impacts of atmospheric rivers over the central United States. *Water Resources Research*, *53*(2), 1144–1166. https://doi.org/10.1002/2016WR019033

Nayak, M. A., & Villarini, G. (2018). Remote sensing-based characterization of rainfall during atmospheric rivers over the central United States. *Journal of Hydrology*, *556*, 1038–1049. https://doi.org/10.1016/j.jhydrol.2016.09.039

Neiman, P. J., Ralph, F. M., Wick, G. A., Lundquist, J. D., & Dettinger, M. D. (2008). Meteorological characteristics and overland precipitation impacts of atmospheric rivers affecting the west coast of North America based on eight years of SSM/I satellite observations. *Journal of Hydrometeorology*, *9*(1), 22–47. https://doi.org/10.1175/2007JHM855.1

Neiman, P. J., Schick, L. J., Ralph, F. M., Hughes, M., & Wick, G. A. (2011). Flooding in western Washington: The connection to atmospheric rivers. *Journal of Hydrometeorology*, *12*(6), 1337–1358. https://doi.org/10.1175/2011JHM1358.1

Newell, R. E., Newell, N. E., Zhu, Y., & Scott, C. (1992). Tropospheric rivers? – A pilot study. *Geophysical Research Letters*, *19*(24), 2401–2404. https://doi.org/10.1029/92GL02916

O'Brien, T. A., Risser, M. D., Loring, B., Elbashandy, A. A., Krishnan, H., Johnson, J., et al. (2020). Detection of atmospheric rivers with inline uncertainty quantification: TECA-BARD v1.0.1. *Geoscientific Model Development*, *13*(12), 6131–6148. https://doi.org/10.5194/gmd-13-6131-2020

Pasquier, J. T., Pfahl, S., & Grams, C. M. (2019). Modulation of atmospheric river occurrence and associated precipitation extremes in the North Atlantic region by European weather regimes. *Geophysical Research Letters*, *46*(2), 1014–1023. https://doi.org/10.1029/2018GL081194

Payne, A. E., Demory, M.-E., Leung, L. R., Ramos, A. M., Shields, C. A., Rutz, J. J., et al. (2020). Responses and impacts of atmospheric rivers to climate change. *Nature Reviews Earth & Environment*, *1*(3), 143–157. https://doi.org/10.1038/s43017-020-0030-5

Ralph, F. M., & Dettinger, M. D. (2011). Storms, floods, and the science of atmospheric rivers. *Eos, Transactions American Geophysical Union*, *92*(32), 265–266. https://doi.org/10.1029/2011EO320001

Ralph, F. M., Dettinger, M. D., Cairns, M. M., Galarneau, T. J., & Eylander, J. (2018). Defining "atmospheric river": How the glossary of meteorology helped resolve a debate. *Bulletin of the American Meteorological Society*, *99*(4), 837–839. https://doi.org/10.1175/BAMS-D-17-0157.1

Ralph, F. M., Iacobellis, S. F., Neiman, P. J., Cordeira, J. M., Spackman, J. R., Waliser, D. E., et al. (2017). Dropsonde observations of total integrated water vapor transport within North Pacific atmospheric rivers. *Journal of Hydrometeorology*, *18*(9), 2577–2596. https://doi.org/10.1175/JHM-D-17-0036.1

Ralph, F. M., Wilson, A. M., Shulgina, T., Kawzenuk, B., Sellars, S., Rutz, J. J., et al. (2019). ARTMIP-early start comparison of atmospheric river detection tools: How many atmospheric rivers hit northern California's Russian River watershed? *Climate Dynamics*, *52*(7), 4973–4994. https://doi.org/10.1007/s00382-018-4427-5

Ramseyer, C. (2021). ERA5 derived integrated water vapor transport for eastern and central U.S. [Data set]. University Libraries, Virginia Tech. https://doi.org/10.7294/15125586.V1

Ramseyer, C. (2022). Atmospheric Rivers of the Eastern U.S. [Data set]. University Libraries, Virginia Tech. https://doi.org/10.7294/20558580

Rutz, J. J., Shields, C. A., Lora, J. M., Payne, A. E., Guan, B., Ullrich, P., et al. (2019). The atmospheric river tracking method intercomparison project (ARTMIP): Quantifying uncertainties in atmospheric river climatology. *Journal of Geophysical Research: Atmospheres*, *124*(24), 13777–13802. https://doi.org/10.1029/2019JD030936

Rutz, J. J., Steenburgh, W. J., & Ralph, F. M. (2014). Climatological characteristics of atmospheric rivers and their inland penetration over the western United States. *Monthly Weather Review*, *142*(2), 905–921. https://doi.org/10.1175/MWR-D-13-00168.1

Sellars, S. L., Gao, X., & Sorooshian, S. (2015). An object-oriented approach to investigate impacts of climate oscillations on precipitation: A western United States case study. *Journal of Hydrometeorology*, *16*(2), 830–842. https://doi.org/10.1175/JHM-D-14-0101.1

Sharma, A. R., & Déry, S. J. (2020). Contribution of atmospheric rivers to annual, seasonal, and extreme precipitation across British Columbia and southeastern Alaska. *Journal of Geophysical Research: Atmospheres*, *125*(9), e2019JD031823. https://doi.org/10.1029/2019JD031823

Shearer, E. J., Nguyen, P., Sellars, S. L., Analui, B., Kawzenuk, B., Hsu, K., & Sorooshian, S. (2020). Examination of global midlatitude atmospheric river lifecycles using an object-oriented methodology. *Journal of Geophysical Research: Atmospheres*, *125*(22), e2020JD033425. https://doi.org/10.1029/2020JD033425

Sheridan, S. C., & Lee, C. C. (2011). The self-organizing map in synoptic climatological research. *Progress in Physical Geography: Earth and Environment*, *35*(1), 109–119. https://doi.org/10.1177/0309133310397582

Shields, C. A., Rutz, J. J., Leung, L.-Y., Ralph, F. M., Wehner, M., Kawzenuk, B., et al. (2018). Atmospheric river tracking method intercomparison project (ARTMIP): Project goals and experimental design. *Geoscientific Model Development*, *11*(6), 2455–2474. https://doi.org/10.5194/gmd-11-2455-2018

Slinskey, E. A., Loikith, P. C., Waliser, D. E., Guan, B., & Martin, A. (2020). A climatology of atmospheric rivers and associated precipitation for the seven U.S. National Climate Assessment Region. *Journal of Hydrometeorology*, *21*(11), 2439–2456. https://doi.org/10.1175/JHM-D-20-0039.1

Smeed, D. A., Josey, S. A., Beaulieu, C., Johns, W. E., Moat, B. I., Frajka-Williams, E., et al. (2018). The North Atlantic Ocean is in a state of reduced overturning. *Geophysical Research Letters*, *45*(3), 1527–1533. https://doi.org/10.1002/2017GL076350

Smeed, D. A., McCarthy, G. D., Cunningham, S. A., Frajka-Williams, E., Rayner, D., Johns, W. E., et al. (2014). Observed decline of the Atlantic meridional overturning circulation 2004–2012. *Ocean Science*, *10*(1), 29–38. https://doi.org/10.5194/os-10-29-2014

Stanley, T. A., Kirschbaum, D. B., Sobieszczyk, S., Jasinski, M. F., Borak, J. S., & Slaughter, S. L. (2020). Building a landslide hazard indicator with machine learning and land surface models. *Environmental Modelling & Software*, *129*, 104692. https://doi.org/10.1016/j.envsoft.2020.104692

Teale, N., & Robinson, D. A. (2020). Patterns of water vapor transport in the eastern United States. *Journal of Hydrometeorology*, *21*(9), 2123–2138. https://doi.org/10.1175/JHM-D-19-0267.1

Teale, N., & Robinson, D. A. (2022). Eastern US precipitation investigated through patterns of moisture transport. *Physical Geography*, *0*(0), 1–25. https://doi.org/10.1080/02723646.2022.2042916

Vesanto, J., Himberg, J., Alhoniemi, E., & Parhankangas, J. (2000). *SOM Toolbox for Matlab 5. Technical Report*. Helsinki University of Technology. Retrieved from https://www.cis.hut./projects/somtoolbox/

Villarini, G. (2016). On the seasonality of flooding across the continental United States. *Advances in Water Resources*, *87*, 80–91. https://doi.org/10.1016/j.advwatres.2015.11.009

Wu, X.-Y., Ye, C., He, W., Chen, J., Xu, L., Zhang, H., et al. (2020). Atmospheric rivers impacting mainland China and Australia: Climatology and interannual variations. *Journal of Southern Hemisphere Earth Systems Science*, *70*(1), 70–87. https://doi.org/10.1071/ES19029

Wu, Y., Jia, Y., Ji, R., & Zhang, J. (2020). SST warming in recent decades in the Gulf Stream extension region and its impact on atmospheric rivers. *Atmosphere*, *11*(10), 1109. https://doi.org/10.3390/atmos11101109

Zhou, Y., O'Brien, T. A., Ullrich, P. A., Collins, W. D., Patricola, C. M., & Rhoades, A. M. (2021). Uncertainties in atmospheric river lifecycles by detection algorithms: Climatology and variability. *Journal of Geophysical Research: Atmospheres*, *126*(8), e2020JD033711. https://doi.org/10.1029/2020JD033711

Zhu, Y., & Newell, R. E. (1998). A proposed algorithm for moisture fluxes from atmospheric rivers. *Monthly Weather Review*, *126*(3), 725–735. https://doi.org/10.1175/1520-0493(1998)126<0725:apafmf>2.0.co;2